Journal of Solid State Chemistry 181 (2008) 1977–1982

Contents lists available at ScienceDirect

Journal of Solid State Chemistry

journal homepage: www.elsevier.com/locate/jssc

Synthesis, structure and physical properties of LnNi(Sn,Sb)$_3$ (Ln = Pr, Nd, Sm, Gd, Tb)

Dixie P. Gautreaux [a], Cigdem Capan [b], John F. DiTusa [b], David P. Young [b], Julia Y. Chan [a,*]

[a] Department of Chemistry, Louisiana State University, 232 Choppin Hall, Baton Rouge, Louisiana 70803, USA
[b] Department of Physics and Astronomy, Louisiana State University, Baton Rouge, Louisiana 70803, USA

ARTICLE INFO

Article history:
Received 21 September 2007; received in revised form 11 April 2008
Accepted 27 April 2008
Available online 4 May 2008

Keywords:
Beta LnNiSb$_3$
LnNi(Sn, Sb)$_3$
PrNi(Sn, Sb)$_3$
NdNi(Sn, Sb)$_3$
SmNi(Sn, Sb)$_3$
GdNi(Sn, Sb)$_3$
TbNi(Sn, Sb)$_3$
CeNiSb$_3$
LaPdSb$_3$
Single crystal
Rare-earth antimonides
Tin flux
X-ray diffraction
Magnetism

ABSTRACT

Five new analogues of the β-CeNiSb$_3$ family have been synthesized and found to be LnNi(Sn,Sb)$_3$ and isostructural to the previously reported β-CeNiSb$_3$. LnNi(Sn,Sb)$_3$ (Ln = Pr, Nd, Sm, Gd, or Tb) crystallizes in the orthorhombic space group, *Pbcm*, with lattice parameters of a~12.9 Å, b~6.1 Å, c~12.0 Å. The structure consists of layers of nearly square nets of X (X = Sn/Sb) atoms and highly distorted NiX_6 octahedra. Lanthanide atoms are located between layers of X and NiX_6 octahedra. All analogues are metallic and experimental effective magnetic moments are in agreement with the respective Ln^{3+} calculated moments.

1. Introduction

Ternary rare-earth antimonides show unusual bonding and interesting physical properties such as large magnetoresistance (MR) and heavy fermion behavior [1–4]. The systematic studies of these ternary phases allow correlation of structure and properties. Structural features such as two-dimensional square sheets or nets and highly layered structures promote unusual physical properties [5]. The La, Ce, Pr, Nd and Sm analogues of LnCrSb$_3$, which crystallize in the orthorhombic space group *Pbcm* with lattice parameters of a~12 Å, b~6 Å, c~6 Å, each display two different magnetic transitions due to the Cr and lanthanide sublattices [6–11]. However, the Gd, Tb and Dy analogues of LnCrSb$_3$ each show only one magnetic transition due to the lanthanide [7,12,13]. YbCrSb$_3$, where Yb is divalent, was found to have a long range ferromagnetic ordering at T_C~280 K [14]. α-CeNiSb$_3$, which crystallizes in the orthorhombic space group *Pbcm* with lattice parameters of a~12 Å, b~6 Å, c~18 Å, orders ferromagnetically at 6 K while the other lanthanide analogues of α-LnNiSb$_3$ (Ln = Pr, Nd and Sm) order antiferromagnetically below 5 K [15–17]. The Dy and Ho analogues of the layered LnNiSb$_2$ display large magnetoresistance (MR) ~115% and~165%, respectively, while the Y analogue is linear up to ~150% at 3 K and 9 T [18].

Tin flux was used in our efforts to grow larger crystals of CeNiSb$_3$ for magnetic and transport measurements and a new polymorph of this phase was discovered, known as β-CeNiSb$_3$ [19]. β-CeNiSb$_3$ adopts the CePdSb$_3$ structure type with the orthorhombic space group *Pbcm* and lattice parameters a~12 Å, b~6 Å, c~12 Å [20,21]. β-CeNiSb$_3$ orders ferromagnetically below 6 K and Kondo lattice behavior is observed [19]. To determine the structural stability of this structure type, we grew several lanthanide analogues. The crystal growth, structure, magnetic properties of LnNi(Sn,Sb)$_3$ (Ln = Pr, Nd, Sm, Gd, Tb) are reported herein.

2. Experimental

2.1. Synthesis

Single crystals of LnNi(Sn,Sb)$_3$ (Ln = Pr, Nd, Sm, Gd or Tb) were prepared using excess Sn as the flux. Pr, Nd, Sm, Gd or Tb pieces

* Corresponding author. Fax: +1 225 578 3458.
E-mail address: jchan@lsu.edu (J.Y. Chan).

0022-4596/$ - see front matter © 2008 Elsevier Inc. All rights reserved.
doi:10.1016/j.jssc.2008.04.029

(99.9%, Alfa Aesar), Ni powder (99.999%, Alfa Aesar), Sb shot (99.999%, Alfa Aesar) and Sn shot (99.8%, Alfa Aesar) were placed in an alumina crucible in a 1:2:3:15 molar ratio. The crucible was sealed into an evacuated fused-silica tube. The reaction vessel was heated to 1150 °C where the temperature was held constant for 24 h and then cooled 5 °C h^{-1} to 300 °C. After dwelling at 300 °C, the excess Sn flux was removed by centrifugation. The reaction mixtures contained silver plate-like crystals with dimensions up to $0.08 \times 3 \times 5\,mm^3$ for all analogues except Tb which contained plate-like crystals with dimensions up to $0.08 \times 0.5 \times 0.5\,mm^3$. Most samples also contained silver rod shaped crystals with dimensions of $1 \times 1 \times 5\,mm^3$. The plates were determined to be the desired product, while the predominant phase is the rod-shaped binary, Ni_3Sn_4. When exposed to air and moisture, there is no visible surface degradation to both compounds over a period of months. Flux growth syntheses with other molar ratios such as 1:1:3:20 and 1:1:3:15 for the latter rare-earth analogues were investigated; however, yield was less than 10%. The addition of excess Ni (1:2:3:15) resulted in an increased yield of *Ln*Ni(Sn,Sb)$_3$. We note that smaller lanthanide metals, Dy and Yb, yielded binary phases.

2.2. Single crystal X-ray diffraction

A typical crystal with dimensions of $\sim 0.08 \times 0.08 \times 0.1\,mm^3$ was mounted onto a glass fiber of a goniometer with epoxy and placed on a Nonius Kappa CCD X-ray diffractometer (Mo$K\alpha$ = 0.71073 Å). Data collection parameters and crystallographic data are listed in Table 1 for *Ln*Ni(Sn,Sb)$_3$ (*Ln* = Pr, Sm, Gd, Tb). The unit cell parameters were determined from images taken at a rotation of 15° φ. The model of the structure was refined by direct methods using SHELXL97 [22]. The data were corrected for absorption and the displacement parameters were refined as anisotropic. Atomic coordinates and anisotropic displacement parameters are provided in Table 2. The R-factors for all compounds are reasonable. We note that the full structure determination for NdNi(Sn,Sb)$_3$ is not included because after multiple data collections, it was determined that this analogue has lower crystal quality based on higher χ^2 values. The lattice parameters are included for comparison purposes.

2.3. Elemental analysis

Elemental analysis using EDX was performed using a Hitachi S-3600N variable pressure scanning electron microscope (VP-SEM) and a stoichiometry of *Ln*NiSnSb$_2$ was obtained; however, Sn and Sb cannot be distinguished accurately using this technique. Elemental analysis of the Sn:Sb composition of the crystals was performed using optical emission spectroscopy (ICP-OES) on a Perkin Elmer Optima Model 5300V for all analogues (Pr, Nd, Sm, Gd, Tb). The Sn:Sb compositions obtained for each analogue are as follows: Pr–$Sn_{0.97}Sb_{2.03}$, Nd–$Sn_{0.92}Sb_{2.08}$, Sm–$Sn_{1.24}Sb_{1.76}$, Gd–$Sn_{0.99}Sb_{2.01}$, Tb–$Sn_{0.59}Sb_{2.41}$. This confirms the presence of Sn in the structure.

2.4. Physical property measurements

Magnetic measurements on single crystals of *Ln*Ni(Sn,Sb)$_3$ oriented in the same direction were performed using a quantum design MPMS superconducting quantum interference device (SQUID) magnetometer. Temperature-dependent susceptibility data were measured with applied fields of 0.1, 0.5, 1 or 5 T from 2 to 300 K. Magnetization as a function of field was measured up to 5 T at 4 or 5 K. The resistivity (between 2 and 300 K) and MR (up to 9 T) was measured on single crystals employing the standard four wires and AC lock-in techniques (with thin Pt wires attached using silver epoxy) in a quantum design physical property measurement system (PPMS) at ambient pressure.

3. Results and discussion

3.1. Structure

*Ln*Ni(Sn,Sb)$_3$ (*Ln* = Pr, Nd, Sm, Gd, Tb) crystallizes in the $CePdSb_3$ structure type with lattice parameters *a*∼12 Å, *b*∼6 Å, *c*∼12 Å [21]. The use of Sn flux allowed crystal growth to occur

Table 1
Crystallographic data for *Ln*Ni(Sn,Sb)3 (*Ln*—Pr, Sm, Gd or Tb)

Formula	$PrNi(Sn,Sb)_3$	$SmNi(Sn,Sb)_3$	$GdNi(Sn,Sb)_3$	$TbNi(Sn,Sb)_3$
Formula units (amu)	561.79	571.24	578.13	579.81
Space group	*Pbcm*	*Pbcm*	*Pbcm*	*Pbcm*
a (Å)	12.843(3)	12.651(1)	12.565(2)	12.450(1)
b (Å)	6.105(7)	6.083(2)	6.072(3)	6.060(2)
c (Å)	12.056(6)	11.994(2)	11.973(4)	11.935(2)
V (Å^3)	945.3(12)	923.0(3)	913.5(6)	900.5(3)
Crystal size (mm^3)	0.01/0.04/0.05	0.01/0.03/0.05	0.02/0.05/0.05	0.01/0.03/0.06
Z	8	8	8	8
Temperature (°C)	24(2)	25(2)	25(2)	25(2)
Density (g cm^{-1})	7.938	8.266	8.452	8.599
θ Range (deg)	3.17–30.08	3.22–30.04	3.25–29.98	3.27–30.01
μ (mm^{-1})	30.747	33.655	35.670	37.163
R_{int}	0.0610	0.0629	0.0557	0.0478
Collected reflections	2541	2492	2434	2469
Unique reflections	1439	1400	1377	1380
h	$-17 \leqslant h \leqslant 17$	$-17 \leqslant h \leqslant 17$	$-17 \leqslant h \leqslant 17$	$-17 \leqslant h \leqslant 17$
k	$-8 \leqslant k \leqslant 8$	$-8 \leqslant k \leqslant 8$	$-8 \leqslant k \leqslant 8$	$-8 \leqslant k \leqslant 8$
l	$-16 \leqslant l \leqslant 16$	$-16 \leqslant l \leqslant 16$	$-16 \leqslant l \leqslant 16$	$-16 \leqslant l \leqslant 16$
$\Delta\rho_{max}$ (e Å^{-3})	4.551	6.822	8.931	7.860
$\Delta\rho_{min}$ (e Å^{-3})	−3.704	−12.674	−8.063	−12.168
Extinction coefficient	0.00050(10)	0.0064(5)	0.00057(19)	0.0064(5)
$R[F^2 > 2\sigma(F^2)]$[a]	0.0522	0.0745	0.0855	0.0618
$wR_2(F^2)$[b]	0.1314	0.1832	0.2092	0.1621

[a] $R_1(F =) \sum ||F_0| - |F_c|| \sum |F_0|$.

[b] $R_w(F_0^2 =) \sum[w(F_0^2 - F_c^2)] \Big/ \sum w(F_0^2)^2]^{1/2}$; $w = 1/[\sigma^2(F_0^2)+(0.0697P)^2+8.8849P]$, $w = 1/[\sigma^2(F_0^2)+(0.1232P)^2+2.3454P]$, $w = 1/[\sigma^2(F_0^2)+(0.1586P)^2]$, $w = 1/[\sigma^2(F_0^2)+(0.1078P)^2+9.3692P]$ for Pr, Sm, Gd and Tb, respectively.

Table 2
Atomic positions and displacement parameters for *Ln*Ni(Sn,Sb)3 (*Ln* = Pr, Sm, Gd or Tb; *X* = Sn/Sb)

Atom	Wyckoff site	*x*	*y*	*z*	U_{eq} (Å^2)[a]
Pr1	4*c*	0.69919(7)	$\frac{1}{4}$	0	0.0123(3)
Pr2	4*d*	0.30501(7)	0.26236(17)	$\frac{3}{4}$	0.0120(3)
Ni1	8*e*	0.10491(13)	0.0301(3)	0.86371(14)	0.0146(4)
*X*1	4*c*	0.97501(10)	$\frac{1}{4}$	0	0.0164(3)
*X*2	4*d*	0.78459(9)	0.2512(2)	$\frac{3}{4}$	0.0131(3)
*X*3	8*e*	0.50157(6)	0.50801(14)	0.87592(6)	0.0130(3)
*X*4	4*c*	0.22006(9)	$\frac{1}{4}$	0	0.0126(3)
*X*5	4*d*	0.94559(9)	0.8841(2)	$\frac{3}{4}$	0.0167(3)
Sm1	4*c*	0.69875(6)	$\frac{1}{4}$	0	0.0078(3)
Sm2	4*d*	0.30574(6)	0.26435(13)	$\frac{3}{4}$	0.0078(3)
Ni1	8*e*	0.10733(10)	0.0297(2)	0.86354(11)	0.0092(4)
*X*1	4*c*	0.97476(8)	$\frac{1}{4}$	0	0.0107(3)
*X*2	4*d*	0.77989(9)	0.25034(14)	$\frac{3}{4}$	0.0081(3)
*X*3	8*e*	0.50213(4)	0.50858(11)	0.87599(6)	0.0090(3)
*X*4	4*c*	0.22485(9)	$\frac{1}{4}$	0	0.0079(3)
*X*5	4*d*	0.94515(7)	0.88488(16)	$\frac{3}{4}$	0.0106(3)
Gd1	4*c*	0.69800(8)	$\frac{1}{4}$	0	0.0077(4)
Gd2	4*d*	0.30634(8)	0.26474(17)	$\frac{3}{4}$	0.0077(4)
Ni1	8*e*	0.10870(16)	0.0295(3)	0.86342(14)	0.0103(5)
*X*1	4*c*	0.97487(11)	$\frac{1}{4}$	0	0.0115(4)
*X*2	4*d*	0.77844(12)	0.2497(2)	$\frac{3}{4}$	0.0086(4)
X3	8*e*	0.50226(7)	0.50904(15)	0.87588(7)	0.0099(4)
*X*4	4*c*	0.22648(12)	$\frac{1}{4}$	0	0.0081(4)
*X*5	4*d*	0.94488(11)	0.8846(2)	$\frac{3}{4}$	0.0116(4)
Tb1	4*c*	0.69785(7)	$\frac{1}{4}$	0	0.0068(3)
Tb2	4*d*	0.30665(7)	0.26545(13)	$\frac{3}{4}$	0.0064(3)
Ni1	8*e*	0.11013(12)	0.0288(3)	0.86377(12)	0.0085(4)
*X*1	4*c*	0.97497(9)	$\frac{1}{4}$	0	0.0097(3)
*X*2	4*d*	0.77590(10)	0.24843(16)	$\frac{3}{4}$	0.0073(3)
*X*3	8*e*	0.50259(5)	0.50885(12)	0.87582(6)	0.0075(3)
*X*4	4*c*	0.22913(10)	$\frac{1}{4}$	0	0.0070(3)
*X*5	4*d*	0.94480(8)	0.88451(18)	$\frac{3}{4}$	0.0106(3)

[a] U_{eq} is defined as one-third of the trace of the orthogonalized U_{ij} tensor.

over a greater temperature range thus stabilizing the new compounds. The structure of $PrNi(Sn,Sb)_3$ is shown in Fig. 1. Because we cannot determine the exact location of Sn within the structure, the nomenclature *X*, where *X* = Sn/Sb, will be used to refer to the main group site. This structure consists of layers of nearly square sheets of *X* atoms, with a layer of square anti-prismatic LnX_8 and mono-capped square anti-prismatic LnX_9 both above and below the Sn/Sb square sheets. There are *Ln* atoms in the capping position of LnX_8 square anti-prisms; however, the inter-atomic distance is too far to be considered bonding. Layers of distorted face- and edge-sharing NiX_6 octahedra are located next to the *Ln* layers. These compounds with lattice parameters ~12 × 6 × 12 Å are related to the α-*Ln*$NiSb_3$ (~12 × 6 × 18 Å) structure type and the main variation is in the stacking of the transition metal subunits [6,15,19].

A decrease in volume is consistent with lanthanide contraction. This was also observed in the α-*Ln*$NiSb_3$ analogues (*Ln*—Ce, Pr, Nd, Sm) [17]. Fig. 2 displays the *Ln*–*X* distances between the *Ln* atoms and *X*-sheets for both α-*Ln*$NiSb_3$ and *Ln*$Ni(Sn,Sb)_3$ as a function of ionic radii. As the lanthanide radii decreases, the distance between the *Ln* atoms and Sb or Sn/Sb nets decreases. Selected interatomic distances of *Ln*$Ni(Sn,Sb)_3$ (*Ln* = La–Nd, Sm, Gd or Tb) are shown in Table 3. As expected, the *Ln*–*X* distances along the *a*-axis decrease as a function of smaller lanthanide. In *Ln*$Ni(Sn,Sb)_3$, the Sn/Sb net layer is formed by four-bonded *X*3 atoms while in the α-phase, the Sb square net is formed by four

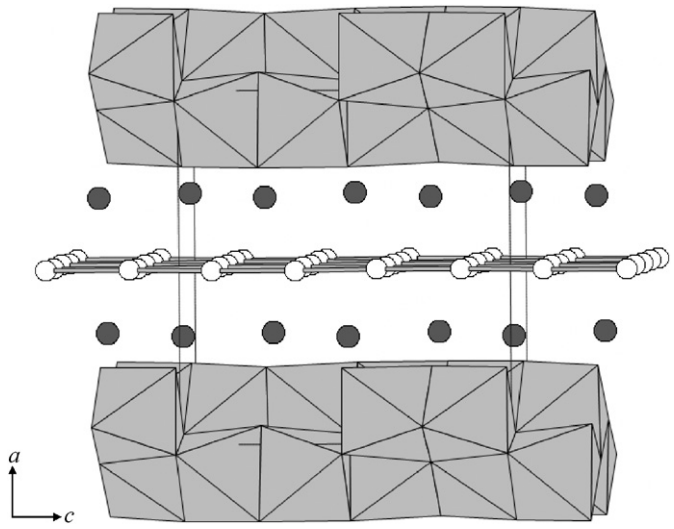

Fig. 1. The structure of $PrNi(Sn,Sb)_3$ viewed down the *b*-axis. The shaded spheres represent Pr atoms, white spheres represent Sn/Sb atoms and shaded polyhedra represent Ni octahedra.

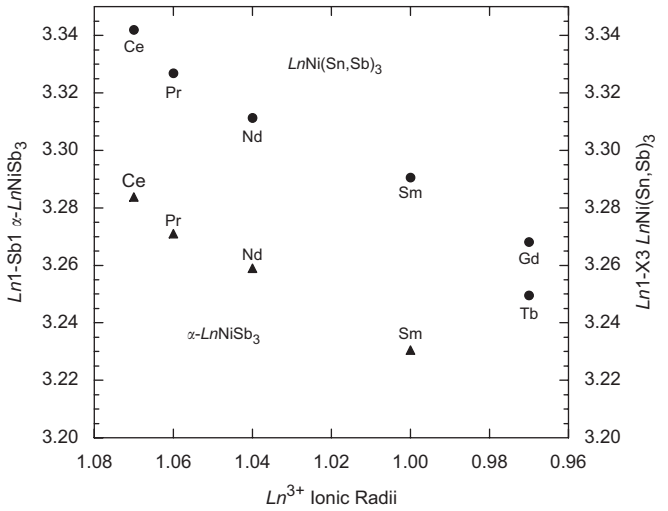

Fig. 2. Plot of *Ln*–*X* (*X* = Sn/Sb) distances as a function of lanthanide for both α-*Ln*$NiSb_3$ and *Ln*$Ni(Sn,Sb)_3$.

Sb1 and Sb3 atoms and is highly distorted [15]. As smaller lanthanides are substituted into the structure, the *X*–*X* distances within the sheets decrease slightly, and the angles are slightly more distorted. Under our growth conditions, the *Ln*$Ni(Sn,Sb)_3$ phase can be adopted for Ce, Pr, Nd, Sm, Gd and Tb while only Ce, Pr, Nd and Sm analogues can be adopted for the α-*Ln*$NiSb_3$ structure type. This may be due to the decrease in lanthanide to Sb net distances, leading to a strain on the structure type.

3.2. Physical properties

The magnetic susceptibility (χ vs *T*) measured at applied fields of 0.1, 0.5, 1 or 5 T for several single crystals of $PrNi(Sn,Sb)_3$, $NdNi(Sn,Sb)_3$, $SmNi(Sn,Sb)_3$ and $GdNi(Sn,Sb)_3$, respectively are shown in Fig. 3. The magnetic field is applied parallel to the *bc*—plane of the crystals. The properties of $TbNi(Sn,Sb)_3$ were not measured due to small yield. A summary of the resulting magnetic data and fit parameters are shown in Table 4. $PrNi(Sn,Sb)_3$ does

Table 3
Selected interatomic distances (Å) of *Ln*Ni(Sn,Sb)3 (*Ln* = Pr, Sm, Gd or Tb; *X* = Sn/Sb)

	$PrNi(Sn,Sb)_3$	$SmNi(Sn,Sb)_3$	$GdNi(Sn,Sb)_3$	$TbNi(Sn,Sb)_3$
*Ln*1–*X*1	3.5423(17)	3.4918(12)	3.4789(17)	3.4501(14)
*Ln*1–*X*2 (× 2)	3.2074(15)	3.1693(6)	3.1593(11)	3.1380(7)
*Ln*1–*X*3 (× 2)	3.3269(15)	3.2906(9)	3.2681(13)	3.2496(10)
*Ln*1–*X*3 (× 2)	3.3408(15)	3.2976(9)	3.2759(13)	3.2506(10)
*Ln*1–*X*4 (× 2)	3.224(3)	3.1914(11)	3.1808(15)	3.1634(11)
*Ln*2–*X*2	3.198(4)	3.1485(15)	3.131(2)	3.1021(16)
*Ln*2–*X*2	3.326(4)	3.3091(15)	3.304(2)	3.2974(16)
*Ln*2–*X*3 (× 2)	3.2994(16)	3.2575(9)	3.2351(13)	3.2115(10)
*Ln*2–*X*3 (× 2)	3.3055(15)	3.2654(9)	3.2453(13)	3.2221(10)
*Ln*2–*X*4 (× 2)	3.2063(15)	3.1695(7)	3.1582(11)	3.1374(7)
*Ln*2–*X*5	3.3032(17)	3.2576(12)	3.2394(17)	3.2126(13)
*X*3–*X*3	2.994(2)	2.9772(14)	2.9748(19)	2.9667(15)
*X*3–*X*3	3.036(2)	3.0221(15)	3.0142(19)	3.0034(15)
*X*3–*X*3	3.053(4)	3.0420(10)	3.0365(15)	3.0307(10)
Ni–*X*1	2.584(2)	2.5790(15)	2.580(2)	2.5730(17)
Ni–*X*1	2.699(2)	2.6997(15)	2.701(2)	2.6968(17)
Ni–*X*2	2.606(2)	2.6033(16)	2.596(2)	2.5968(18)
Ni–*X*4	2.586(2)	2.5857(15)	2.580(2)	2.5760(17)
Ni–*X*5	2.619(2)	2.6153(15)	2.618(2)	2.6163(18)
Ni–*X*5	2.641(3)	2.6390(17)	2.636(2)	2.638(2)
Ni–Ni	2.742(4)	2.724(3)	2.716(3)	2.716(3)

not appear to order down to 2 K. However, the possibility remains that this sample may order below 2 K as signs of ordering can be seen in the magnetization near 2 K. An effective moment of 3.65 μ_B and a Weiss temperature (θ) of ~−1 K were obtained from a modified Curie Weiss fit ($\chi = \chi_0 + C/(T+\theta)$) between 100 and 300 K. The μ_{eff} of 3.68 μ_B is slightly larger than the calculated moment of 3.57 μ_B for the Pr^{3+} ion and is consistent with the magnetic contribution coming solely from the Pr. $NdNi(Sn,Sb)_3$ is paramagnetic down to 2 K. Fits to the inverse susceptibility between 2 and 300 K reveal an effective moment of 3.93 μ_B and a Weiss temperature, θ ~−4 K. The experimental moment of 3.93 μ_B is slightly larger than the calculated moment of 3.62 μ_B for the Nd^{3+} ion. $SmNi(Sn,Sb)_3$ appears be paramagnetic down to 2.5 K. An effective moment of 0.65 μ_B and a Weiss temperature (θ) of ~−19 K were obtained with a Curie–Weiss fit from 50 to 300 K. The experimental moment is slightly smaller than the expected moment of 0.84 μ_B for Sm^{3+}. $GdNi(Sn,Sb)_3$ is also paramagnetic down to 2 K and an effective moment of 7.47 μ_B and a Weiss temperature (θ) of ~−403 K were obtained from the modified Curie–Weiss fit. The expected moment for Gd^{3+} is 7.94 μ_B which is slightly larger than the experimental moment. The fact that these analogues (Pr, Nd, Sm, Gd) do not seem to order while β-$CeNiSb_3$ orders ferromagnetically at 6 K, and α-*Ln*$NiSb_3$ orders antiferromagnetically for *Ln* = Pr, Nd, Sm with $T_{Neel} \leqslant 5$ K, is quite surprising [19]. The evolution of the Curie–Weiss temperatures (except Gd) follows the de Gennes factors across the *Ln* series as expected [23], and are close to the values found in the α-analogues. The susceptibility deviates from the free-ion Curie–Weiss behavior at low temperatures which may be due to crystalline electric field effect. Further work is needed to clarify the possible role of dimensionality and geometrical frustration in destabilizing the long range magnetic order in the structure as well as to determine the crystalline electric field ground state scheme.

The magnetization of single crystals of $PrNi(Sn,Sb)_3$, $NdNi(Sn,Sb)_3$, $SmNi(Sn,Sb)_3$ and $GdNi(Sn,Sb)_3$ as a function of field (*M* vs *H*) at temperatures of 5 or 4 K is shown in Fig. 4. The magnetization of $PrNi(Sn,Sb)_3$ begins to show signs of saturation at around 4 T, well below the theoretical saturation moment of 3.2 μ_B. The difference points to the importance of short range correlations in the proximity of a magnetic instability in this

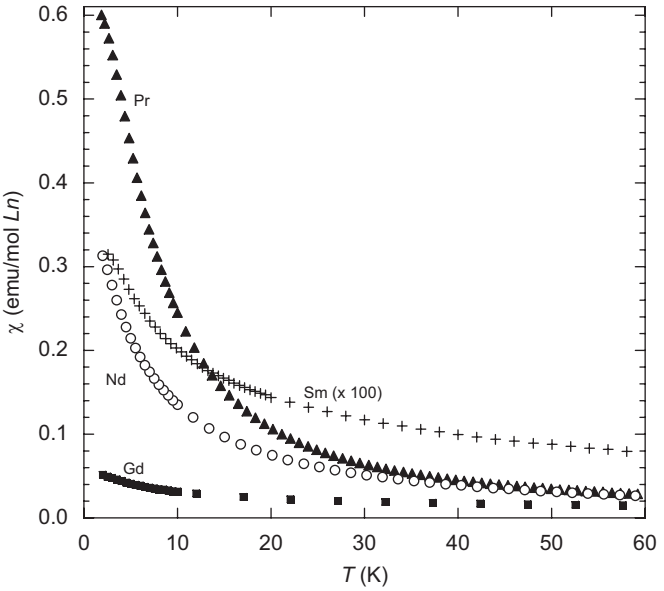

Fig. 3. Magnetic susceptibility as a function of temperature between 2 and 300 K for $PrNi(Sn,Sb)_3$ ($H = 0.1$ T), $NdNi(Sn,Sb)_3$ ($H = 0.5$ T), $SmNi(Sn,Sb)_3$ ($H = 1$ T) and $GdNi(Sn,Sb)_3$ ($H = 1$ T) where the triangles, open circles, crosses and squares refer to $PrNi(Sn,Sb)_3$, $NdNi(Sn,Sb)_3$, $SmNi(Sn,Sb)_3$ and $GdNi(Sn,Sb)_3$, respectively. The data for $SmNi(Sn,Sb)_3$ has been multiplied by 100 to fit the scale.

Table 4
Summary of magnetic susceptibility data

	$PrNi(Sn,Sb)_3$	$NdNi(Sn,Sb)_3$	$SmNi(Sn,Sb)_3$	$GdNi(Sn,Sb)_3$
H (T)	1	0.5	1	1
Temperature Range (K)	100–300	2–300	50–300	150–300
χ_0	−0.0001	−0.0035	0.000937	−0.00059
C	1.69	1.93	0.053	6.94
θ (K)	−0.97	−3.92	−19.33	−403.51
μ_{calc} (μ_B)	3.57	3.62	0.84	7.94
μ_{eff} (μ_B)	3.68	3.93	0.65	7.45

compound, as also evidenced by the anomalous behavior of resistivity (see below). The magnetization for the other analogues is nearly linear up to fields of 5 T. The diamagnetic background contribution is less than 3% of the total signal for all samples. Moreover, the magnetization values at 5 T are consistent with the corresponding α-analogues, suggesting similar magneto-crystalline anisotropy and crystal field splitting in both structure types. The magnetization of the Gd-analogue, however, is anomalously small. This, coupled to the small effective moment, suggests either a strong anisotropy or partial screening of the Gd moments by conduction electrons.

The resistivity as a function of temperature for *Ln*$Ni(Sn,Sb)_3$ (*Ln* = Pr, Nd, Sm, Gd) is displayed in Fig. 5. The current was applied parallel to the *bc*—plane of the crystals. All analogues display simple metallic behavior with a small ratio of room temperature to low temperature resistivity. The Ce analogue displays metallic Kondo behavior, with a resistivity minimum around 20 K and a pronounced drop below the Curie temperature (6 K) while the La analogue displays simple metallic behavior [19]. The resistivity of the Ce analogue differs slightly from the previous report and is more representative of the compound. There is also a superconducting transition seen in all samples ~3.5 K which we attribute to Sn flux on the surface of the crystals (not shown). We also note that the resistivity of the Pr analogue has a quasi-linear temperature dependence below 50 K. This, together with a small

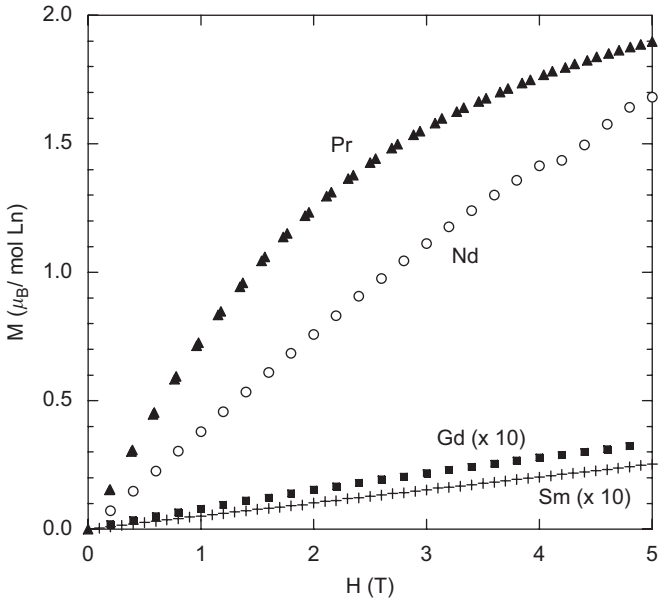

Fig. 4. Field-dependent magnetization of single crystals of $PrNi(Sn,Sb)_3$ ($T = 5$ K) and $NdNi(Sn,Sb)_3$ ($T = 4$ K), $SmNi(Sn,Sb)_3$ ($T = 4$ K) and $GdNi(Sn,Sb)_3$ ($T = 4$ K) where the triangles, open circles, crosses and squares refer to $PrNi(Sn,Sb)_3$, $SmNi(Sn,Sb)_3$, $NdNi(Sn,Sb)_3$ and $GdNi(Sn,Sb)_3$, respectively The data for the Sm- and Gd-analogues have been multiplied by 10 to fit the scale.

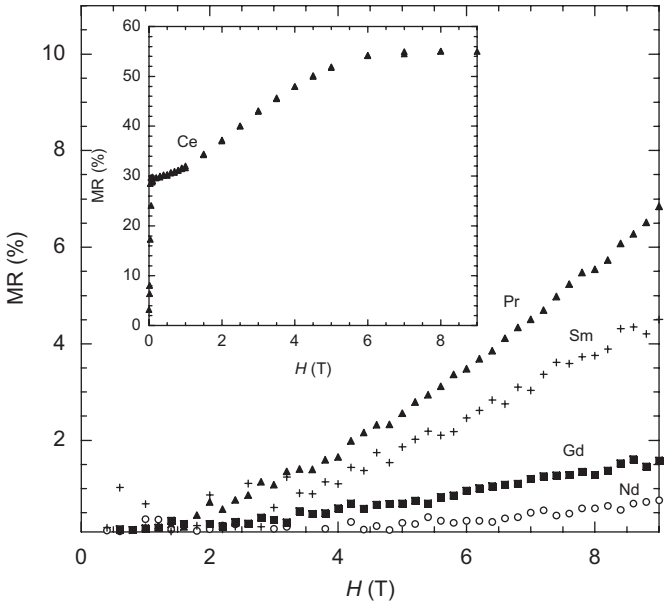

Fig. 6. Magnetoresistance of single crystals of β-$LaNiSb_3$ (3 K), β-$CeNiSb_3$ (3 K), $PrNi(Sn,Sb)_3$ (5 K), $NdNi(Sn,Sb)_3$ (5 K), $SmNi(Sn,Sb)_3$ (5 K) and $GdNi(Sn,Sb)_3$ (5 K). The open triangles, open diamonds, triangles, open circles, crosses and squares refer to refer to β-$LaNiSb_3$, β-$CeNiSb_3$, $PrNi(Sn,Sb)_3$, $NdNi(Sn,Sb)_3$, $SmNi(Sn,Sb)_3$ and $GdNi(Sn,Sb)_3$, respectively. The data for β-$CeNiSb_3$ is located in the inset.

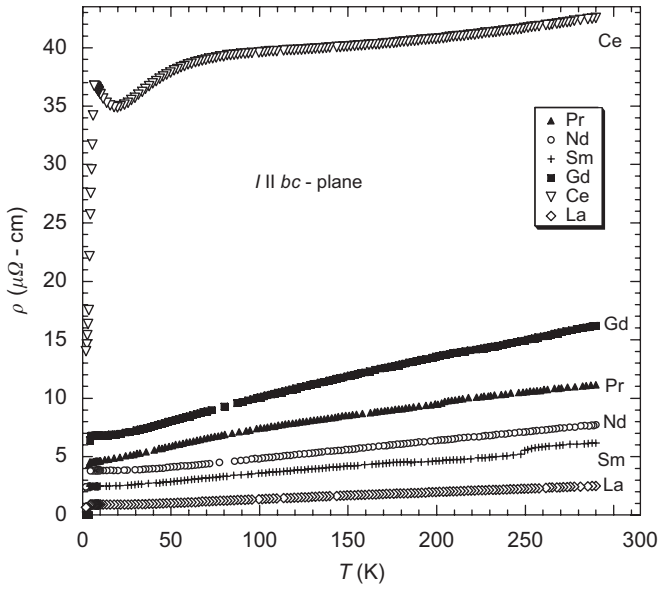

Fig. 5. Temperature-dependent resistivity of single crystals of $LnNi(Sn,Sb)_3$ (Ln = La, Ce, Pr, Nd, Sm, Gd) where the open triangles, open diamonds, triangles, open circles, crosses and squares refer to β-$LaNiSb_3$, β-$CeNiSb_3$, $PrNi(Sn,Sb)_3$, $NdNi(Sn,Sb)_3$, $SmNi(Sn,Sb)_3$ and $GdNi(Sn,Sb)_3$, respectively.

Curie–Weiss temperature, suggests that $PrNi(Sn,Sb)_3$ is close to a magnetic instability.

The MR as a function of field for $LnNi(Sn,Sb)_3$ (Ln = Pr, Nd, Sm, Gd) is shown in Fig. 6. All analogues show a small positive MR at $T = 5$ K with a nearly quadratic field dependence and no signs of saturation up to 9 T, with a similar magnitude as the La analogue. This indicates that the MR is mostly dominated by the positive contribution, although one cannot exclude that a small negative contribution, due to the quenching of spin fluctuations by magnetic field, still persists at low temperatures. Indeed, the MR at $H = 9$ T changes sign upon warming and a negative MR is recovered at temperatures above 100 K in all compounds (not shown). Assuming localized *f*-electrons, these compounds should have a similar density of charge carriers. In this case, the difference between the compounds is presumably due to the interplay between the orbital and the spin contributions. In contrast, the positive MR in the magnetic phase of β-$CeNiSb_3$ at $T = 3$ K, above the saturation field, also shown in Fig. 6, is an order of magnitude larger and saturates around 6 T. The positive non-saturating MR is reminiscent of other planar materials including structurally related $LnSb_2$ (Ln = La, Pr, Sm, Nd) whose structure also contains square Sb sheets; however, the analogues investigated here have a significantly smaller MR than these other compounds [24].

Acknowledgments

We thank Amar Karki of the Department of Physics and Astronomy at Louisiana State University for useful discussion. J.Y.C. acknowledges the NSF-CAREER (DMR 0237664) and Alfred P. Sloan Fellowship for partial support of this project. J.F.D. acknowledges the support of the NSF through DMR 0406140. D.P.Y. gratefully acknowledges support from NSF (Grant DMR 0449022).

References

[1] A.M. Mills, R. Lam, M.J. Ferguson, L. Deakin, A. Mar, Coord. Chem. Rev. 233–234 (2002) 207–222.
[2] O. Sologub, P.S. Salamakha, K.A. Gschneidner, J.C.G. Bunzli, V.K. Pecharsky, Handbook on the Physics and Chemistry of Rare Earths, vol. 33, Elsevier, Netherlands, 2003.
[3] S.M. Kauzlarich, S.M. Kauzlarich, Chemistry, Structure, and Bonding in Zintl Phases and Ions, VCH Publishers, New York, 1996.
[4] E. Bauer, N.A. Frederick, P.C. Ho, V.S. Zapf, M. Maple, Phys. Rev. B 65 (2002) 100506(R).
[5] G.A. Papoian, R. Hoffmann, Angew. Chem. Int. Ed. 39 (2000) 2409–2448.
[6] K. Hartjes, W. Jeitschko, M. Brylak, J. Magn. Magn. Mater. 173 (1997) 109–116.

[7] M. Leonard, S. Saha, N. Ali, J. Appl. Phys. 85 (1999) 4561–4759.
[8] M.L. Leonard, I.S. Dubenko, N. Ali, J. Alloys Compd. 303–304 (2000) 265–269.
[9] D.D. Jackson, M. Torelli, Z. Fisk, Phys. Rev. B 65 (2001) 014421.
[10] L. Deakin, M.J. Ferguson, A. Mar, Chem. Mater. 13 (2001) 1407–1412.
[11] D.D. Jackson, Z. Fisk, J. Magn. Magn. Mater. 256 (2003) 106–116.
[12] D.D. Jackson, Z. Fisk, J. Alloys Compd. 377 (2004) 243–247.
[13] L. Deakin, A. Mar, Chem. Mater. 15 (2003) 3343–3346.
[14] S.J. Crerar, L. Deakin, A. Mar, Chem. Mater. 17 (2005) 2780–2784.
[15] R.T. Macaluso, D.M. Wells, R.E. Sykora, T.E. Albrecht-Schmitt, A. Mar, S. Nakatsuji, H. Lee, Z. Fisk, J.Y. Chan, J. Solid State Chem. 177 (2004) 293–298.
[16] V.A. Siderov, E.D. Bauer, H. Lee, S. Nakatsuji, J.D. Thompson, Z. Fisk, Phys. Rev. B 71 (2005) 094422-1–094422-4.
[17] E.L. Thomas, R.T. Macaluso, H. Lee, Z. Fisk, J.Y. Chan, J. Solid State Chem. 177 (2004) 4228–4236.
[18] E.L. Thomas, M. Moldovan, D.P. Young, J.Y. Chan, Chem. Mater. 17 (2005) 5810–5816.
[19] E.L. Thomas, D.P. Gautreaux, H.O. Lee, Z. Fisk, J.Y. Chan, Inorg. Chem. 46 (2007) 3010–3016.
[20] A. Thamizhavel, H. Nakashima, T. Shiromoto, Y. Obiraki, T.D. Matsuda, Y. Haga, S. Ramakrishnan, T. Takeuchi, R. Settai, Y. Onuki, J. Phys. Soc. Jpn. 74 (2005) 2617–2621.
[21] E.L. Thomas, D.P. Gautreaux, J.Y. Chan, Acta Crystallogr. Sect. E Struct. Rep. E 62 (2006) i96–i98.
[22] G.M. Sheldrick, University of Gottingen, Germany, 1997.
[23] J. Jensen, A.R. Mackintosh, Rare Earth Magnetism Structure and Excitations, Clarendon Press, Oxford, 1991.
[24] S.L. Bud'ko, P.C. Canfield, C.H. Mielke, A.H. Lacerda, Phys. Rev. B 57 (1998) 13624–13638.